Fuel 427 (2027) 139560

Contents lists available at ScienceDirect

Fuel

journal homepage: www.elsevier.com/locate/jfue

Full length article

Comparison of point-particle models and direct particle-fluid simulations for non-spherical particles

Laurent André[a,*], Thede Kiwitt[a], Matthias Meinke[a,b], Dominik Krug[a], Wolfgang Schröder[a,b]

[a] Chair of Fluid Mechanics and Institute of Aerodynamics, RWTH Aachen University, Wüllnerstr. 5a, 52062 Aachen, Germany
[b] JARA Center for Simulation and Data Science, RWTH Aachen University, Seffenter Weg 23, 52074 Aachen, Germany

HIGHLIGHTS

- Pipe and free jet simulations laden with heavy rigid non-spherical particles.
- Spherical and ellipsoidal particles with aspect ratios $1 \leq \beta \leq 8$.
- Large eddy simulations at a bulk Reynolds number of $Re_D = 15\,000$.
- Spherical and ellipsoidal point-particle models are investigated.
- Point-particle simulations are compared to direct particle-fluid simulations.

ARTICLE INFO

Keywords:
Particle-laden turbulent flow
Coupled pipe-jet simulations
Euler-Lagrange models
Direct particle-fluid simulations
Non-spherical particles

ABSTRACT

Coupled particle-laden pipe and free jet simulations are performed at a Reynolds number of $Re_D = 15\,000$ based on the nozzle diameter. The flow is laden with heavy rigid spherical and prolate particles, with aspect ratios in the range of $1 \leq \beta \leq 8$ typically found in the context of bio-mass oxy-fuel combustion. A fully developed turbulent periodic pipe flow with a volume loading of $\phi_v = 6.67 \cdot 10^{-4}$ supplies the inflow for the free jet through a slicing technique, thereby ensuring consistent inflow conditions for the fluid and dispersed phases. An Euler-Lagrange approach is used for the simulations, where a large-eddy simulation is performed for the carrier flow and individual particles, represented by point masses, are tracked in a Lagrangian frame. Three different point-particle models are used. A conventional spherical model, an ellipsoidal model derived for creeping flow conditions, and an ellipsoidal model that includes orientation-dependent correlations for drag, lift, and torque valid for finite particle Reynolds numbers. In this study, results from the point-particle models are compared with interface-resolved direct particle-fluid simulations (DPFS) and the predictive capability and accuracy of each model are assessed. Discrepancies in the wall-bounded pipe flow are discussed and improvements concerning, e.g., the collision model and the limitations of the correlations derived under the assumption of uniform flow are outlined. Within the jet, the extended ellipsoidal model shows good agreement with the DPFS data for the translational particle motion, radial spreading, and preferential orientation.

1. Introduction

Particle-laden flows are of great relevance in natural phenomena and technical applications. Examples range from atmospheric events such as dust storms [1], over sediment transport in riverbeds [2] to industrial systems such as the combustion of solid fuels [3].

The latter represents the particular application addressed in this manuscript. In solid-fuel combustion, solid particles, serving as energy carriers, are transported by a gaseous flow. With an ever-growing global energy demand [4], the search for cleaner and sustainable combustion concepts is of utmost importance and ongoing. One promising route is to replace fossil fuels, for instance coal, with renewable alternatives such as pulverized biomass and to retrofit existing power plants with carbon capture and utilization technologies [4].

Due to their fibrous nature, biomass particles typically exhibit an anisotropic shape, a feature far less pronounced in coal particles. Indeed, biomass particles are better approximated by cylinders or ellipsoids than

* Corresponding author.
Email address: l.andre@aia.rwth-aachen.de (L. André).

https://doi.org/10.1016/j.fuel.2026.139560
Received 28 October 2025; Received in revised form 3 March 2026; Accepted 17 April 2026
Available online 27 April 2026

Nomenclature

List of Abbreviations

DPFS	direct particle-fluid simulation
EELM	extended ellipsoidal Lagrangian model
ELM	ellipsoidal Lagrangian model
ODF	orientation distribution function
PDF	probability density function
PPS	point-particle simulation
SLM	spherical Lagrangian model
SP	single-phase

List of Symbols

β	aspect ratio
d_{eq}	volume equivalent diameter
μ	dynamic viscosity
Re_p	particle Reynolds number
ϕ	inclination angle
Re_D	bulk Reynolds number
$\rho,\ \rho_p$	fluid and particle densities
$\mathbf{u},\ \mathbf{u}_p$	fluid and particle velocities
$\boldsymbol{\omega}$	angular particle velocity
$\mathbf{F}_p$	hydrodynamic force
$\mathbf{T}_p$	hydrodynamic torque
$\phi_v,\ \phi_m$	volume and mass loadings
D	pipe diameter
d_p	spherical diameter
u_b	bulk velocity
u_c	centerline velocity
u_{rad}	radial velocity

spheres [5]. Such a non-spherical shape leads to notably different behavior in particle-laden flows. In particular the particle orientation, and therefore the rotational dynamics, becomes a relevant aspect [6], whereas the impact of rotational motion is often negligible for spherical particles [7]. Consequently, the particle orientation should be taken into consideration when modeling the motion of non-spherical particles.

For the simulation of full-scale furnaces, direct particle-fluid simulations (DPFS), in which all scales are resolved, are prohibitively expensive. A computationally more affordable alternative is Euler-Lagrange simulations, in which large-eddy simulations (LES) for the carrier phase are coupled with the Lagrangian tracking of individual point-like particles [8]. The forces acting on the point masses are obtained from empirical or semi-empirical correlations that usually depend on the particle shape and flow regime. The overall accuracy of the simulation critically depends on the fidelity of the particle model.

The motion of spherical particles in such models is well understood and can be described by models such as the Maxey-Riley equation [9], including corrections for finite particle Reynolds numbers [8].

Analytical solutions for non-spherical particles under creeping flow conditions have been available for decades, covering the hydrodynamic force [10] as well as the torque [11] and have been applied in numerous studies [12–15]. However, these models neglect finite particle Reynolds number effects and are formally only valid in the limit of $Re_p \to 0$.

More recently, several authors have proposed extended models for different shapes, including corrections for finite particle Reynolds numbers [16–19]. For example, the model by Zastawny et al. [16] has been applied in [20] for channel flows with non-spherical particles, revealing a preferential orientation of the particles with their major axes perpendicular to the local flow direction. The ellipsoidal model by Fröhlich et al. [19] was used to investigate the settling behavior of prolate particles in decaying isotropic turbulence [21], revealing a preferential alignment of the particles' major axes perpendicular to the settling direction.

These findings highlight the importance of incorporating the particle shape into the modeling approaches. Despite the prevalence of non-spherical particles in biomass applications, spherical point-particle models are commonly used due to their simplicity and broad availability within simulation frameworks. However, to the best of the authors' knowledge, no systematic assessment of a turbulent free jet laden with ellipsoidal particles is available that compares:

(a) a purely spherical point-particle model,
(b) an ellipsoidal point-particle model without,
(c) and an ellipsoidal model with orientation-dependent correlations for the drag, lift, and torque coefficients.

Therefore, a canonical configuration relevant to biomass combustion, has been selected for the current investigation. The objective of this discussion is to assess the accuracy of the three point-particle models and to benchmark them against direct particle-fluid simulation reference data obtained for the same investigated configuration [6]. The present study extends previous results on isotropic turbulence [15] by directly contrasting, for the first time, the extended ellipsoidal point-particle model, including the correlations proposed by Fröhlich et al. [19] for prolate particles at finite Re_p, against reference DPFS. Moreover, the chosen configuration is an important step towards more practically relevant applications by assessing different point-particle models in turbulent pipe and free-jet flows, which more closely resemble the conditions found in a burner. Consequently, the questions targeted in this work concern the reliability and limitations of point-particle modeling as typically applied in simulations of biomass oxy-fuel combustion and widely used in the design and analysis of combustion processes.

Since experimental data on the particle dynamics of non-spherical particles in turbulent free-jet flows are not available in the literature the DPFS serves as reference data for the Lagrangian point-particle models. The DPFS has been thoroughly validated for various flow problems in [22–24].

The focus is on heavy prolate particles whose aspect ratios are in the range of $1 \leq \beta \leq 8$ with an equivalent volume diameter of $d_{\mathrm{eq}}/D = 0.01$. These aspect ratios align with those documented in the literature for pulverized biomass [25]. The bulk jet Reynolds number based on the nozzle diameter D is $Re_D = 15\,000$.

Although the present work is motivated by combustion applications, chemical reactions and heat transfer are deliberately excluded to isolate shape effects and will be investigated in future research, i.e., this study is restricted to the dynamics of rigid spherical and ellipsoidal particles.

The manuscript is organized as follows. Section 2 reviews the governing equations for the fluid and particle phases, followed by the numerical methodology in Section 3. Section 4 describes the numerical setup and the investigated flow and particle parameter space. The results are presented and discussed in Section 5, and a brief conclusion is given in Section 6.

2. Mathematical model

In the following, the governing equations for the fluid and dispersed phases are presented.

2.1. Governing equations for the fluid phase

The flow of a compressible viscous fluid is governed by the conservation laws for mass, momentum, and energy. In non-dimensional integral

form and for a control volume V, these equations read

$$\frac{\mathrm{d}}{\mathrm{d}t}\int_V \mathbf{Q}\,\mathrm{d}V + \oint_{\partial V}\left(\underline{\mathbf{H}}^{\mathrm{inv}} - \underline{\mathbf{H}}^{\mathrm{vis}}\right)\cdot\mathbf{n}\,\mathrm{d}A = \int_V \mathbf{F}\mathrm{d}V\,, \tag{1}$$

where ∂V denotes the control volume surface and $\mathbf{n}$ the outward-facing normal vector. The vector of the conservative variables is defined as $\mathbf{Q} = [\rho,\, \rho\,\mathbf{u},\, \rho E]^{\mathrm{T}}$ with the density ρ, the velocity vector $\mathbf{u}$, and the total specific energy E. The flux tensor is decomposed into an inviscid part $\underline{\mathbf{H}}^{\mathrm{inv}}$ and a viscous part $\underline{\mathbf{H}}^{\mathrm{vis}}$ which read

$$\underline{\mathbf{H}}^{\mathrm{inv}} - \underline{\mathbf{H}}^{\mathrm{vis}} = \begin{bmatrix} \rho\,\mathbf{u} \\ \rho\,\mathbf{u}\,\mathbf{u} + p\,\underline{\mathbf{I}} \\ \rho\,E\,\mathbf{u} + p\,\mathbf{u} \end{bmatrix} - \begin{bmatrix} 0 \\ \underline{\boldsymbol{\tau}} \\ \underline{\boldsymbol{\tau}}\,\mathbf{u} + \mathbf{q} \end{bmatrix}, \tag{2}$$

where p is the pressure, $\underline{\mathbf{I}}$ the identity tensor, $\underline{\boldsymbol{\tau}}$ the stress tensor, and $\mathbf{q}$ the vector of heat conduction. The term $\mathbf{F}$ denotes the volume force.

For a Newtonian fluid with vanishing bulk viscosity, the stress tensor $\underline{\boldsymbol{\tau}}$ can be written as

$$\underline{\boldsymbol{\tau}} = \mu\,\left(\nabla\mathbf{u} + (\nabla\mathbf{u})^{T}\right) - \frac{2}{3}\,\mu\,(\nabla\cdot\mathbf{u})\,\underline{\mathbf{I}}\,, \tag{3}$$

where the dynamic viscosity μ is evaluated as a function of the temperature T using Sutherland's law

$$\mu(T) = \frac{T^{3/2}}{Re_0}\,\frac{1+\mathrm{S}_\mu}{T+\mathrm{S}_\mu}\,, \tag{4}$$

with S_μ the Sutherland constant and $Re_0 = \rho_0\,a_0\,L_0/\mu_0$ the Reynolds number based on the stagnation-point reference values of the density ρ_0, the dynamic viscosity μ_0, the speed of sound a_0, and the reference length L_0.

The vector of heat conduction is expressed by Fourier's law

$$\mathbf{q} = -k(T)\,\nabla T\,, \tag{5}$$

where the temperature-dependent thermal conductivity is given by

$$k(T) = \frac{T^{3/2}}{Re_0\,Pr_0\,(\gamma-1)}\,\frac{1+\mathrm{S}_k}{T+\mathrm{S}_k}\,, \tag{6}$$

with the heat-capacity ratio γ, the thermal Sutherland constant S_k, and the constant Prandtl number $Pr_0 = \mu_0\,c_{p,0}/k_0 = 0.72$, where $c_{p,0}$ is the specific heat at constant pressure.

Closure is achieved through the ideal gas law, which reads $\gamma\,p = \rho\,T$ when applying the selected non-dimensionalization using the stagnation point quantities [26].

2.2. Governing equations for the disperse phase

The free motion of a rigid particle with mass m_p is governed by the hydrodynamic force $\mathbf{F}_p$ exerted by the surrounding fluid on the particle surface Γ_p. In this contribution, the gravitational force is omitted to focus on the particle-fluid interaction in a flow field that is characterized by a strong forced convection environment. The translational motion under the neglect of gravity is therefore governed by

$$m_p\,\frac{\mathrm{d}\mathbf{u}_p}{\mathrm{d}t} = \mathbf{F}_p\,, \tag{7}$$

where $\mathbf{u}_p$ denotes the particle velocity. The hydrodynamic force is obtained from the surface integral

$$\mathbf{F}_p = \oint_{\Gamma_p}(-p\,\mathbf{n} + \underline{\boldsymbol{\tau}}\cdot\mathbf{n})\,\mathrm{d}A\,. \tag{8}$$

The rotational motion is formulated in a reference frame that is fixed to the particle and whose axes are aligned with its principal axes of inertia ($\hat{x}$, $\hat{y}$, $\hat{z}$), see Fig. 1. Quantities marked by a hat ($\hat{\cdot}$) are expressed in this particle-fixed frame. The rotational equation of motion in the co-rotating reference frame reads

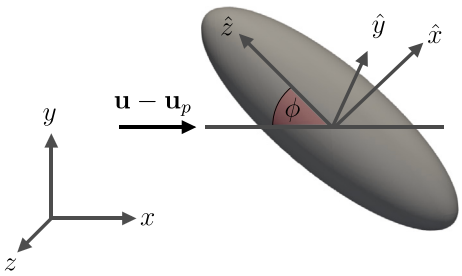

Fig. 1. Schematic of the global reference frame (x, y, z) and the particle fixed frame of reference $(\hat{x}, \hat{y}, \hat{z})$. The particle inclination angle ϕ is defined as the angle between the relative velocity $\mathbf{u}-\mathbf{u}_p$ and the particle's major axis $\hat{\mathbf{z}}$.

$$\hat{\underline{\mathbf{J}}}\,\frac{\mathrm{d}\hat{\boldsymbol{\omega}}}{\mathrm{d}t} + \hat{\boldsymbol{\omega}}\times\left(\hat{\underline{\mathbf{J}}}\,\hat{\boldsymbol{\omega}}\right) = \hat{\mathbf{T}}_p\,, \tag{9}$$

where $\hat{\underline{\mathbf{J}}}$ is the diagonal tensor containing the principal moments of inertia, $\hat{\boldsymbol{\omega}}$ the angular velocity, and $\hat{\mathbf{T}}_p$ the torque exerted by the fluid onto the particle. The torque is computed by

$$\mathbf{T}_p = \oint_{\Gamma_p}(\mathbf{x}_\Gamma - \mathbf{x}_p)\times(-p\,\mathbf{n} + \underline{\boldsymbol{\tau}}\cdot\mathbf{n})\,\mathrm{d}A\,, \tag{10}$$

with $\mathbf{x}_\Gamma$ the position vector on the surface and $\mathbf{x}_p$ the center of mass of the particle.

The orientation of the particle is represented by the vector of quaternions $\boldsymbol{\epsilon} = (\epsilon_0,\, \epsilon_1,\, \epsilon_2,\, \epsilon_3)^{\mathrm{T}}$ [27], which is preferred over Euler angles due to its numerical stability. To prevent the accumulation of numerical errors, the vector of quaternions is renormalized after each time step. Quantities defined in the particle-fixed frame are related to those in the inertial frame through the rotation matrix $\underline{\mathbf{R}}(\boldsymbol{\epsilon})$.

3. Numerical methods

First, the numerical approach for the fluid phase is described. Then, the different modeling approaches for the dispersed phase are described. All simulations are conducted using the simulation framework *m-AIA* (multiphysics-Aerodynamisches Institut Aachen) [28].

3.1. Fluid phase

A finite-volume solver based on hierarchical Cartesian meshes is employed to solve the governing Eq. (1) of the fluid phase [29]. The viscous fluxes are discretized using a central scheme, whereas for the inviscid fluxes an upwind-biased scheme is utilized. Time integration is performed with a five-stage Runge-Kutta scheme [22,30]. The simulation framework includes an automatic mesh generator and supports adaptive mesh refinement (AMR) based on discrete sensors. A dynamic load-balancing strategy [31] ensures an even workload across all computational ranks despite varying computational loads due to the moving particles.

3.2. Disperse phase

The computation of the hydrodynamic force (8) and torque (10) exerted by the fluid on the particle determines the essential difference between the modeling approaches for the dispersed phase. In the following, several approaches — direct particle-fluid simulation and three point-particle models — are briefly described.

3.2.1. Direct particle-fluid simulations (DPFS)

In direct particle-fluid simulations [23] the surfaces of the particles and the surrounding fluid are resolved. In the simulation framework m-AIA, a cut-cell method is used. The particle boundary is described by an analytical level-set, i.e., a signed distance function, and is sharply discretized by the cut-cell formulation [30,32]. This allows the evaluation of the surface integrals (8) and (10) in discrete form as a sum over the individual surface elements. The numerical method has been validated in [22–24] for numerous particle-laden flows. Locally refined meshes around the particles significantly reduce the overall computational cost without compromising accuracy. Multiple level-sets allow the use of multi cut cells, enabling sub-cell resolution of particle-wall and particle-particle interactions. Collisions are handled by an extension for non-spherical particles of the model proposed by Glowinski et al. [33] and are assumed to be fully elastic. A description of the collision handling in the DPFS formulation is given in [6].

3.2.2. Point-particle simulations (PPS)

In contrast to the DPFS approach, point-particle simulations replace each particle with an infinitesimal point carrying the same mass, i.e., a point mass with zero spatial extension. Since the surface is no longer resolved, the momentum and energy exchange with the carrier fluid has to be explicitly modeled.

Typically, this method is valid only when the particles are sufficiently small, i.e., smaller than the smallest turbulent length scale, such that their finite size can be neglected and they can be treated as point masses [8]. Accordingly, a point-particle model is applied to approximate the force and torque terms in (8) and (10).

The influence of the dispersed phase on the carrier flow is modeled through a two-way coupling approach, in which the hydrodynamic force acting on each particle is subtracted from the momentum and energy equations of the fluid by an additional source term [34]. Applying this approach to a single cell, however, results in a locally disturbed flow field, which is not accounted for by the standard point-particle models. In the present work, the flow disturbance is reduced by a smooth distribution [35] of the hydrodynamic force $\mathbf{F}_p$ over the surrounding cells using a distance-weighted projection. The force contribution $\mathbf{F}_{\mathrm{proj},i}$ assigned to the neighbouring cell i reads

$$\mathbf{F}_{\mathrm{proj},i} = \mathbf{F}_p \cdot \frac{\exp\left(r_i^2/(\sigma\Delta^2)\right)}{\sum_i \exp\left(r_i^2/(\sigma\Delta^2)\right)} , \tag{11}$$

where r_i is the distance between the particle center of mass and the center of the cell i, Δ is the local grid size, and σ is a smoothing parameter that controls the extent of the projection kernel [36]. The distribution is performed over two cells wrapped around each particle.

In the simulation framework m-AIA, an efficient parallel coupling between the flow and particle solvers is realised through an interleaved execution pattern. This is facilitated by splitting the solution step into multiple sub-stages of comparable computational load. Together with a non-blocking message passing interface (MPI) communication, the interleaved strategy achieves high parallel efficiency and yields a considerable speed-up compared to a sequential coupling [34].

Particles that impinge on a wall rebound through a reflection model based on a virtual sphere with a radius equivalent to the particle's semi-major axis. The wall normal component of the incoming particle velocity is inverted, simulating a fully elastic rebound, and the new position of the particle is updated accordingly. The rotational motion remains unchanged by the collision. While particle-wall collisions are necessary for the simulation, particle-particle collisions are neglected since the volume loading in the pipe flow is below 1%, which is considered sufficiently low based on the experiences from homogeneous isotropic turbulence [8]. More complex collision models for non-spherical particles have been proposed among others in [37] and [38].

In the remainder of this section, three point-particle models, i.e., the spherical Lagrangian model (SLM), the ellipsoidal Lagrangian model (ELM), and the extended ellipsoidal Lagrangian model (EELM), implemented within the PPS framework, are described. Their accuracy will be analyzed later and the results will be compared with DPFS data whenever such a direct comparison is possible.

Spherical Lagrangian model (SLM). The most basic point-particle model is the classical spherical model, which ignores the anisotropy in the particle shape. The motion of a solid, small, and spherical particle is commonly described by the Maxey-Riley equation [9]. For heavy particles ($\rho_p \gg \rho$) the dominant contributions are the drag and gravitational force [8]. In the present investigation, only the drag term is considered. The Stokes drag is corrected for finite particle Reynolds numbers $Re_p = \rho\,|\mathbf{u} - \mathbf{u}_p|\,d_p/\mu$ such that

$$\mathbf{F}_p = 3\,\pi\,\mu\,f_d\,d_p\,(\mathbf{u} - \mathbf{u}_p) , \tag{12}$$

where f_d is a correction term. In this work the Schiller-Naumann drag correction $f_{d,SN} = 1 + 0.15\,Re_p^{0.687}$ [39] is chosen.

The translational equation of motion (7) is solved using a predictor-corrector scheme [14,27]. The rotational motion is neglected as it is considered to be of minor importance for particles of spherical shape [7].

Ellipsoidal Lagrangian model (ELM). For modeling the dynamics of general ellipsoidal particles, analytical solutions derived under creeping flow conditions are widely used. The translational motion of a rigid ellipsoid is governed by the drag force, which can be expressed by

$$\mathbf{F}_p = \mu\,\underline{\mathbf{R}}^T\,\underline{\hat{\mathbf{K}}}\,\underline{\mathbf{R}}\,(\mathbf{u} - \mathbf{u}_p) , \tag{13}$$

where $\underline{\hat{\mathbf{K}}}$ is a diagonal resistance tensor defined in the particle frame [10].

In creeping shear flow, the torque acting on the ellipsoidal particle relates the strain rate and vorticity of the fluid to the particle's angular velocity [11]. The expression reads

$$\hat{\mathbf{T}}_p = \mu\,\underline{\hat{\mathbf{K}}}_s\,\hat{\mathbf{s}} + \mu\,\underline{\hat{\mathbf{K}}}_\zeta\,(\hat{\boldsymbol{\zeta}} - \hat{\boldsymbol{\omega}}) , \tag{14}$$

where the resistance tensors $\underline{\hat{\mathbf{K}}}_s$ and $\underline{\hat{\mathbf{K}}}_\zeta$ are defined analogously to $\underline{\hat{\mathbf{K}}}$. The strain rate $\hat{\mathbf{s}}$ and vorticity $\hat{\boldsymbol{\zeta}}$ are given in the particle frame by

$$\hat{\mathbf{s}} = \frac{1}{2}\left(\frac{\partial u_{\hat{z}}}{\partial \hat{y}} + \frac{\partial u_{\hat{y}}}{\partial \hat{z}}, \frac{\partial u_{\hat{x}}}{\partial \hat{z}} + \frac{\partial u_{\hat{z}}}{\partial \hat{x}}, \frac{\partial u_{\hat{y}}}{\partial \hat{x}} + \frac{\partial u_{\hat{x}}}{\partial \hat{y}}\right)^{\mathrm{T}} , \tag{15}$$

$$\hat{\boldsymbol{\zeta}} = \frac{1}{2}\left(\frac{\partial u_{\hat{z}}}{\partial \hat{y}} - \frac{\partial u_{\hat{y}}}{\partial \hat{z}}, \frac{\partial u_{\hat{x}}}{\partial \hat{z}} - \frac{\partial u_{\hat{z}}}{\partial \hat{x}}, \frac{\partial u_{\hat{y}}}{\partial \hat{x}} - \frac{\partial u_{\hat{x}}}{\partial \hat{y}}\right)^{\mathrm{T}} . \tag{16}$$

The analytical expressions for the resistance tensors of prolate spheroids are provided in Appendix A.

Extensions of the ELM towards finite particle Reynolds numbers are usually limited to specific shapes and/or flow regimes. In the following, an extended model for prolate particles is described.

Extended ellipsoidal Lagrangian model (EELM). The classical ellipsoidal model has been reformulated and complemented with orientation-dependent correlations for the drag, lift, and torque for prolate ellipsoidal particles in [19]. The correlations include corrections for finite particle Reynolds numbers up to $Re_p = 100$ and are valid for particle aspect ratios $1 \le \beta \le 8$.

The hydrodynamic force defined in the particle fixed coordinate system and depending on the drag and lift coefficient $C_{D,\phi}$ and $C_{L,\phi}$ reads

$$\begin{aligned}\hat{\mathbf{F}}_p = {} & \rho\,\frac{\pi}{8}\,d_{\mathrm{eq}}^2\,\left|\hat{\mathbf{u}} - \hat{\mathbf{u}}_p\right|^2\,C_{D,\phi}(Re_p,\beta)\,\hat{\mathbf{d}}_D \\ & + \rho\,\frac{\pi}{8}\,d_{\mathrm{eq}}^2\,\left|\hat{\mathbf{u}} - \hat{\mathbf{u}}_p\right|^2\,C_{L,\phi}(Re_p,\beta)\,\hat{\mathbf{d}}_L ,\end{aligned} \tag{17}$$

where ϕ is the inclination angle between the particle's major axis $\hat{\mathbf{z}}$ and the direction of the drag force $\hat{\mathbf{d}}_D$. The direction vectors for the drag and

lift force are

$$\hat{\mathbf{d}}_D = \frac{\hat{\mathbf{u}} - \hat{\mathbf{u}}_p}{\left|\hat{\mathbf{u}} - \hat{\mathbf{u}}_p\right|} \quad \text{and} \quad \hat{\mathbf{d}}_L = \hat{\mathbf{d}}_D \times \hat{\mathbf{d}}_T \,, \tag{18}$$

and the torque direction is defined by

$$\hat{\mathbf{d}}_T = \frac{\hat{\mathbf{d}}_D \times \hat{\mathbf{z}}}{\left|\hat{\mathbf{d}}_D \times \hat{\mathbf{z}}\right|} \operatorname{sign}(\hat{\mathbf{d}}_D \cdot \hat{\mathbf{z}}) \,. \tag{19}$$

The orientation-dependent drag coefficient relates the two limiting orientations of 0° and 90° by a sine-square law for intermediate angles, which also holds for higher Re_p [40]

$$C_{D,\phi}(Re_p, \beta) = C_{D,0} + (C_{D,90} - C_{D,0}) \sin^2(\phi) \,, \tag{20}$$

with $C_{D,0}$ and $C_{D,90}$ obtained from the Stokes flow solutions which are corrected for finite Re_p similar to the spherical case

$$C_{D,i}(Re_p, \beta) = C_{D,\mathrm{Stokes},i}(Re_p, \beta)\, f_{d,i}(Re_p, \beta) \,. \tag{21}$$

The lift coefficient is similarly formulated. To reduce systematic deviations for $Re_p > 0$ an additional correction function $\Psi_\phi(Re_p, \beta)$ for the inclination angle is introduced

$$C_{L,\phi}(Re_p, \beta) = 2 \sin(\Psi_\phi) \cos(\Psi_\phi)\, C_{L,\max}(Re_p, \beta) \,. \tag{22}$$

Eq. (14) for the torque is extended by a pitching torque component that rotates the particles towards their most stable orientation $\phi \to 90°$ [19] such that

$$\hat{\mathbf{T}}_p = \mu\, \underline{\hat{\mathbf{K}}}_s\, \hat{\mathbf{s}} + \mu\, \underline{\hat{\mathbf{K}}}_\zeta\, (\hat{\boldsymbol{\zeta}} - \hat{\boldsymbol{\omega}}) + \rho\, \frac{\pi}{16}\, d_{\mathrm{eq}}^3 \left|\hat{\mathbf{u}} - \hat{\mathbf{u}}_p\right|^2 C_{T,\phi}(Re_p, \beta)\, \hat{\mathbf{d}}_T \,. \tag{23}$$

As the pitching term vanishes for $Re_p \to 0$, the torque coefficient is not obtained by a simple correction from the Stokes flow expressions but is directly modeled as

$$C_{T,\phi}(Re_p, \beta) = 2 \sin(\phi) \cos(\phi)\, C_{T,\max}(Re_p, \beta) \,. \tag{24}$$

The details of the correction functions $f_{d,i}$ and Ψ_ϕ as well as the maximum lift coefficient $C_{L,\max}$ and torque coefficient $C_{T,\max}$ are provided in Appendix B and a detailed description is available in [19].

4. Numerical setup

A turbulent free jet is investigated coupled to a fully developed turbulent pipe flow that provides the inflow conditions. The numerical setup consists of two separate computational domains: one for the pipe flow and one for the free jet. Both simulations run concurrently and are one-way coupled via a slicing technique. That is, at every time step a cross-section of the pipe flow solution is extracted and imposed as the inflow condition for the jet. The domains overlap in a short region where the two computational grids coincide. Within this region, the data transfer reduces to an in-memory copy, eliminating any need for interpolation. The impact of prescribing a fully developed pipe flow as inflow on the subsequent jet development has been analyzed by Nguyen and Oberlack [41]. It has been shown that a fully developed turbulent pipe flow as inlet distribution reduces the potential core length such that the velocity decay occurs further upstream.

The same approach also yields the inflow condition for the dispersed phase, i.e., particle positions, orientations, and translational as well as rotational velocities are transferred. Further details are given in [6]. Consequently, consistent inflow conditions are ensured for both the fluid and particle phases. An overview of the configuration, which is described in more detail in [6], is shown in Fig. 2.

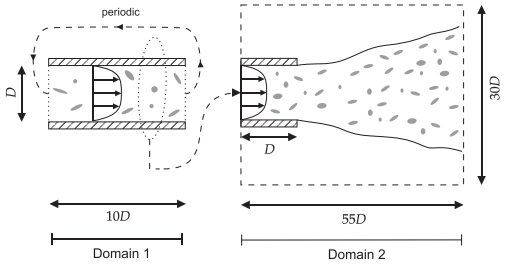

Fig. 2. Schematic of the numerical setup showing the extent of the pipe flow and jet domains together with the slicing technique used to transfer the information from the turbulent pipe flow to the inlet of the jet.

4.1. Computational domain and boundary conditions

For the pipe flow simulation, periodic boundary conditions are imposed in the streamwise direction. At the pipe wall a no-slip condition is imposed. A domain length of $L = 10\,D$ is chosen, which is sufficiently long to capture the largest turbulent structures and to avoid artifacts introduced by the periodicity [42].

For the jet simulation, a rectangular domain measuring $L_x = 55\,D$ in the streamwise direction and $L_y = L_z = 30\,D$ in the lateral directions is used. The pipe extends $1\,D$ into the jet domain where the inner and outer radii of the pipe are explicitly modeled. At the downstream and lateral boundaries, boundary conditions of Neumann type are prescribed for velocity and density, whereas the pressure is relaxed to the ambient value.

A locally refined mesh is employed, with the finest cells located near the wall, at the outlet and in the near-field. The mesh is gradually coarsened further downstream of the jet. For the point-particle simulations, a near-wall resolution of $y^+ \approx 2$ is achieved. The combined grid contains approximately $6.2 \cdot 10^8$ grid cells, about 521 million cells of which are used to resolve the jet and 97 million cells for the pipe flow. The DPFS have a particle resolution of $d_{\mathrm{eq}}/\Delta_{min} = 14$ and a near wall resolution of $y^+ \approx 1.22$. For the details of the DPFS, including the reference results used in this discussion, the reader is referred to [6].

4.2. Flow and particle parameters

The simulations are performed at a bulk Reynolds number of

$$Re_D = \frac{\rho_j\, u_b\, D}{\mu_j} = 15\,000 \,, \tag{25}$$

where D denotes both the pipe and nozzle exit diameter, u_b the bulk velocity at the exit, ρ_j and μ_j the density and dynamic viscosity at the jet inflow cross-section. For the pipe flow, this corresponds to a friction Reynolds number of

$$Re_\tau = \frac{u_\tau D}{\nu} = 448 \,, \tag{26}$$

with the friction velocity $u_\tau = \sqrt{\tau_w/\rho}$ where τ_w is the wall-shear stress and ν the kinematic viscosity. The Mach number of the flow is $Ma = 0.1$.

The particles are initialized in the pipe domain at random positions and with random orientations. The prolate spheroids are characterized by their semi-minor axes $a = b$ and semi-major axis c such that the aspect ratio is given by $\beta = c/a$. Aspect ratios in the range of $1 \le \beta \le 8$ are investigated with an equal distribution of particles for each value, i.e., 12.5% of the total number of particles per aspect ratio. All particles share the same volume-equivalent diameter $d_{\mathrm{eq}}/D = 0.01$, where $d_{\mathrm{eq}} = 2\,a\,\beta^{1/3}$. Motivated by biomass particles [5], a density ratio of $\rho_p/\rho = 600$ is prescribed. Each particle has identical mass. This ensures that differences in the results are reduced to the particle geometry. A total of 10,000 particles are initialized within the pipe domain, yielding a

Table 1
Overview of the flow and particle parameter space.

Parameter	Value
Bulk Reynolds Number Re_D	15 000
Friction Reynolds Number Re_τ	448
Mach Number Ma	0.1
Diameter d_{eq}/D	0.01
Density Ratio ρ_p/ρ	600
Stokes Number St	50
Aspect Ratio β	{1, 2, 3, 4, 5, 6, 7, 8}
Probability $P(\beta = i)$	12.5%
Volume Loading ϕ_v	$6.67 \cdot 10^{-4}$
Mass Loading ϕ_m	0.4

volume loading of $\phi_v \approx 6.67 \cdot 10^{-4}$ and a mass loading of $\phi_m \approx 0.4$. Since streamwise periodic boundary conditions are imposed, the particle count remains constant in the pipe domain. Within the jet domain, the number varies slightly but stays on the order of $\mathcal{O}(10^5)$.

The Stokes number based on the characteristic time scale $t = D/u_b$ is evaluated as

$$St = \frac{Re_D}{18}\frac{\rho_p}{\rho}\left(\frac{d_{eq}}{D}\right)^2 = 50\,. \tag{27}$$

This value indicates that due to the particles' high inertia their response time is substantially greater than the characteristic time of the flow. This ratio of the time scales is particularly relevant when the accuracy of the employed point-particle models due to the inertia determined particle movement is evaluated.

An overview of the flow and particle parameter space is given in Table 1.

5. Results

In this section the time-averaged results for the fluid and particle phases are discussed. The findings in the turbulent pipe flow and the turbulent jet flow are discussed separately from each other. First, the results of the particle-laden pipe flow are presented in Section 5.1, followed by the investigation of the particle-laden jet in Section 5.2.

The focus lies on the predictive capabilities of the different point-particle models. Specifically, differences between the spherical model and the ellipsoidal point-particle approaches will be highlighted. Both the translational and the rotational motions are analyzed and the particle impact on the fluid phase is investigated. Furthermore, the point-particle simulation results are compared with the DPFS results of [6] whenever corresponding DPFS data are available. The single-phase configuration has been validated against numerical and experimental data in [6].

5.1. Particle-laden turbulent pipe flow

The statistical results of the pipe flow solution are independent of the jet flow due to the one-way formulation of the slicing technique. First, the preferential particle concentration is examined, followed by an investigation of the translational and rotational motion.

5.1.1. Spatial particle distribution

The probability density function (PDF) of the radial particle concentration compensated by the bin area reveals a preferential concentration peak near the wall for each of the investigated point-particle models SLM, ELM, and EELM at a location of $r/D = 0.46$ to 0.48 as illustrated by the PDF in Fig. 3(a). This trend is well-known for wall-bounded flows [43] and has also been reported in [6]. The peak for the SLM and EELM is significantly higher than that for the analytical ELM, which lacks corrections for finite particle Reynolds numbers. The ELM exhibits a much more uniform distribution across the full radial distance. The SLM predicts a slight preference, compared with the EELM, for the particles to be located closer to the wall. This behavior is directly related to the applied wall-collision model, which for the EELM is a function of the semi-major axis and the anisotropic shape.

Compared with DPFS results in Fig. 3(b), this peak, however, lies closer to the wall. The point-particle simulations show only minor variations in the peak location as a function of the aspect ratio, whereas the direct particle-fluid simulations in [6] demonstrate that the preferential concentration location moves further away from the wall as the particle aspect ratio increases. While the difference for spherical particles ($\beta = 1$) is already $\approx 26\%$, the deviation grows for larger aspect ratios ($\beta = 8$) to $> 60\%$.

One factor contributing to the reduced sensitivity observed in the PPS is the phenomenon of preferential orientation of the particles' major axes with respect to the streamwise direction. This will be examined in more detail in Section 5.1.3, where significant differences between the ellipsoidal point-particle and DPFS are observed for the pipe flow. Several additional factors may contribute to the deviations. First, the collision model used in the DPFS and PPS differs slightly. Whereas the point-particle approach applies a reflection model in which the particle velocity is inverted, i.e., a reflection model focused on the linear particle dynamics, the DPFS uses a collision model that additionally applies rotational forces based on the contact point of the fully-resolved bodies. For the PPS, an extended algorithm has to be implemented that determines the contact point on the virtual particle outline and thereby allows for eccentric particle collision. Additionally, it is assumed that the locally varying forces from the turbulent structures at the smallest scale have a non-negligible impact on the integrated particle movement. Within the DPFS, all scales are specifically resolved such that local variances along the particle surface are considered. Within the point-particle model, this cannot be taken into account due to the reduction of the particle size. Since the discussed correlation equations are derived in

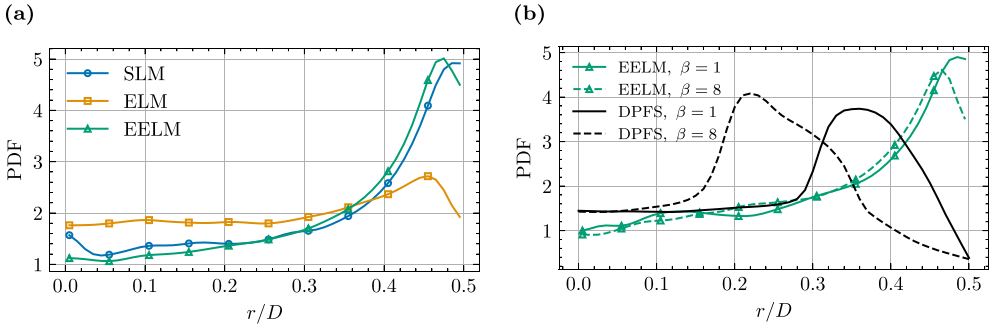

Fig. 3. Probability density function of the radial particle distribution for the pipe flow, (a) average results for the SLM, ELM, and EELM point-particle models for all particles and (b) EELM results and DPFS data [6] for particles with aspect ratios $\beta = 1$ and 8 are compared. The PDF is compensated by the bin area.

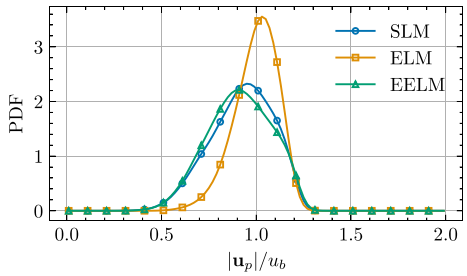

Fig. 4. Probability density function of the particle velocity $|\mathbf{u}_p|/u_b$ for all particles within the pipe flow, different point-particle models are compared.

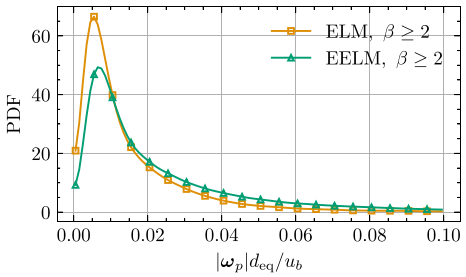

Fig. 6. Probability density function of the angular velocity magnitude $|\boldsymbol{\omega}_p| d_{\mathrm{eq}}/u_b$ for the mean of prolate particles with aspect ratios $\beta \geq 2$ within the pipe flow, ellipsoidal point-particle models are compared.

uniform or creeping flow conditions, no such local variances were considered. This is especially notable in intense shear-driven flows such as in wall-bounded turbulent pipe flow.

5.1.2. Translational particle dynamics

The preferential concentration directly affects the particle velocities shown in Fig. 4. Since the ELM predicts a more uniform radial distribution, more particles reside in the central region of the pipe, where the fluid velocity is maximum. In addition, the drag is underpredicted due to missing finite particle Reynolds number corrections. This results in a PDF peak at a 15% higher particle velocity than for the EELM. The SLM and EELM distributions again show good agreement, with a slightly shifted PDF for the EELM towards lower values.

The behavior in the radial direction is further illustrated by analyzing the spatially and temporally averaged radial velocity u_{rad} in Fig. 5. While the near wall behavior qualitatively agrees with the DPFS data, this is not the case in the pipe center. In Fig. 5(a), the DPFS results show a strong tendency to move away from the center, whereas the point-particle models fail to predict this trend and show a diverging behavior, leading to an overall lower average radial velocity in the center. This result holds for all three point-particle models, as shown in Fig. 5(b). The mean predicted velocity in the radial direction is up to one order of magnitude smaller than for the DPFS results [6]. Despite a global volume loading within the pipe flow below 1%, the local concentration can be higher and increases close to the centerline of the pipe such that the importance of finite-size effects and particle-particle collisions, neglected in the point-particle simulations, grows.

5.1.3. Rotational particle dynamics

The rotational particle dynamics is now investigated for the ELM and EELM, the spherical model is omitted, as it neglects the rotational motion and particle orientation. The analysis of the angular velocity magnitude shows that the additional pitching-torque term in (23) slightly increases the likelihood of higher angular velocity obtained for the EELM relative

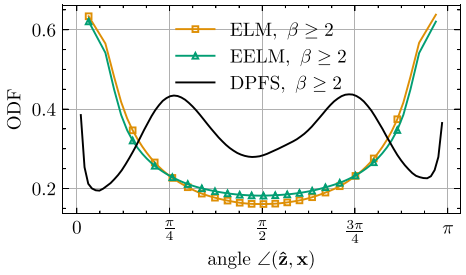

Fig. 7. Orientation distribution function of the particle orientation $\angle(\mathbf{x}, \hat{\mathbf{z}})$ defined by the angle between the streamwise direction $\mathbf{x}$ and the particle's major axis $\hat{\mathbf{z}}$, results for ellipsoidal point-particle models and DPFS [6] for the mean of prolate particles with aspect ratios $\beta \geq 2$ are compared. The DPFS data have been scaled according to the ODF formulation.

to the ELM, as illustrated in Fig. 6. Nevertheless, the angular velocities remain roughly one order of magnitude lower compared to the reported values in [6].

Although the average orientation angle, defined as the angle between the particle's major axis $\hat{\mathbf{z}}$ and the streamwise direction $\mathbf{x}$ is around 52°, the orientation distribution function (ODF) [27], i.e., the compensated probability density function of the orientation computed by non-uniform bins of equal area on the unit sphere, shows a preference for the particles to be oriented in the streamwise direction. This is evident from the peaks at angles of 0° or 180°, i.e., 0 or π, in Fig. 7. This result does not agree with the DPFS data in [6], which indicate preferential orientation peaks at 55° and 125°. It suggests that the added pitching torque in the EELM is not strong enough, compared with the contribution of the velocity gradient, to orient the particles with their major axes perpendicular to the flow. Note that the correlations and finite particle Reynolds number corrections in the EELM are based on uniform flow around fixed prolate particles [19]. Further investigations, particularly

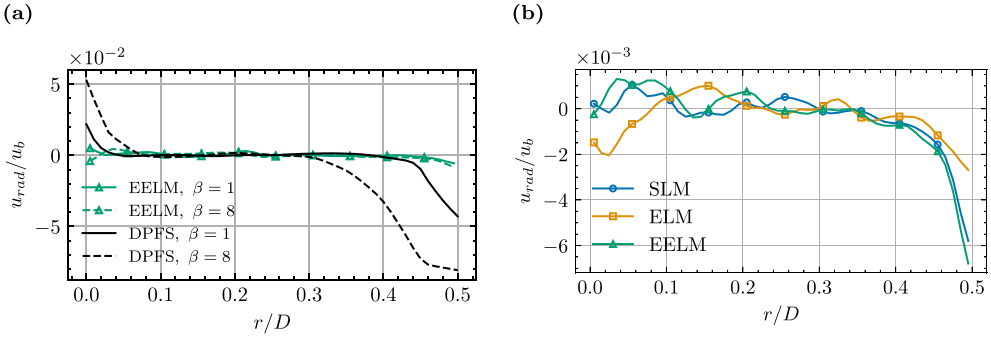

Fig. 5. Radial velocity u_{rad}/u_b as a function of the radial distance r/D from the pipe centerline, (a) EELM results and DPFS data [6] for particles with aspect ratios $\beta = 1$ and $\beta = 8$ and (b) average results for the different point-particle models for all particles are compared.

into the directly modeled pitching torque term, are required to assess and, if necessary, correct the model for strong shear flows.

It is clear that particle-particle and particle-wall collisions influence the orientation and rotational dynamics. In particular, the latter could be described by more realistic, eccentric collisions instead of the simplified spherical reflection model discussed in Section 3.2.2. This would lead to more complex trajectories and additional moments which, in turn, directly affect the translational and rotational motion.

Furthermore, the local impact of the particle-induced dissipation affects the local structure of the turbulent flow. In the direct particle-fluid simulations, the explicit resolution of the particle surfaces and the ensuing computation of the dissipation at the local cell level are in contrast to the distribution of the forces in the two-way coupling point-particle approach. Here, the dissipation is considered by a weighted smoothing kernel that distributes the total dissipation induced by the particle proportionally to all surrounding cells, i.e., local variances in the induced dissipation are not considered.

To summarize, the current analysis highlights the importance of the extended correlations, including finite particle Reynolds number corrections within the ellipsoidal point-particle models, as shown by the strong underprediction of the hydrodynamic forces by the ELM. The differences in the translational motion between the SLM and EELM are small, however, the former neglects the rotational motion. Limitations of the EELM have been identified and the necessity of improvements such as a more realistic collision model and improved finite particle Reynolds number corrections in strong shear flows was discussed.

5.2. Particle-laden turbulent free jet

Next, the overall impact of the particulate phase on the streamwise development of the free jet is analyzed. Subsequently, preferential particle concentration and overall dispersion behavior are presented before the translational and rotational particle dynamics are discussed.

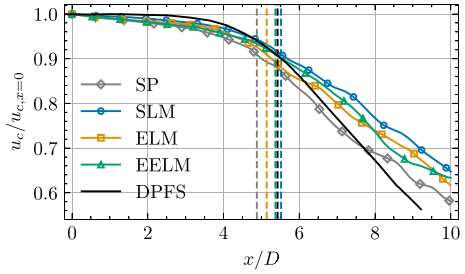

Fig. 8. Decay of the normalized streamwise fluid velocity on the jet centerline $u_c/u_{c,x=0}$, the profiles are based on single-phase (SP), point-particle (SLM, ELM, EELM) and direct particle-fluid simulation (DPFS) data. The vertical lines define the locations where the velocity has decayed to 90% of the inlet value $u_{c,x=0}$.

5.2.1. Free jet development

The impact of the particle phase on the fluid phase is assessed by comparing the time-averaged fluid velocity on the centerline. Fig. 8 shows the single-phase result and the particle-laden solutions, which include the three different point-particle models and the direct particle-fluid simulation. Due to the momentum transfer from the particles, the particle-laden solutions show an increase in the potential-core length compared to the single-phase simulations. This tendency is observed in all different modalities, i.e., all three point-particle models and the DPFS. The potential-core length is highlighted by the vertical lines defined as $u_c/u_{c,x=0} = 0.9$ in Fig. 8.

However, the results indicate that the ELM underpredicts the particle-fluid momentum exchange and hence, it only slightly influences the flow field by increasing the potential-core length by 5%. The EELM and SLM have a stronger impact on the jet development, resulting in an increased potential-core length by 10% and 13%. This agrees very well with the DPFS results [6]. However, for $x/D \leq 5$, the DPFS predicts a higher centerline velocity than the point-particle simulations. Further downstream, for $x/D \geq 7$, a slightly faster decay rate for the DPFS solution than for the single-phase solution is observed, which is likely caused by an increased radial momentum exchange. This development could not be matched by any of the point-particle simulations.

The differences between the point-particle and the direct particle-fluid simulations are further explained by the implemented two-way coupling which only considers the hydrodynamic force, see Section 3.2.2. In the EELM, a portion of the total kinetic energy is transformed into rotational kinetic energy, whereas the SLM considers only the translational motion. Further investigations need to be conducted to evaluate the influence of a torque coupling scheme.

5.2.2. Particle dispersion

In the discussion of the particulate phase, the radial particle dispersion predicted by each point-particle model is investigated first in Fig. 9, in which the radial dispersion as a function of the distance from the nozzle exit is presented for the three point-particle models color-coded by the average aspect ratio. The smallest dispersion is obtained by the ELM. This is due to the larger average particle-velocity already present at the jet inlet. The SLM and EELM show similar results, although the EELM exhibits on average a progressively larger dispersion in the region of $0 \leq x/D \leq 10$. The data show that particles with higher aspect ratios migrate further in the radial direction. For a given positively inclined orientation relative to the flow direction, prolate particles experience a higher lift force resulting in a stronger lateral motion. This factor is also considered one of the reasons for the differences between the SLM and EELM distributions. This effect is further influenced by the velocity gradients and associated shear forces within the turbulent free jet.

Despite the differences in the preferential concentration between the direct particle-fluid simulations and the point-particle simulations in the pipe flow, which define the inflow distributions, a better agreement between PPS and DPFS is obtained for the jet. Nevertheless, the DPFS

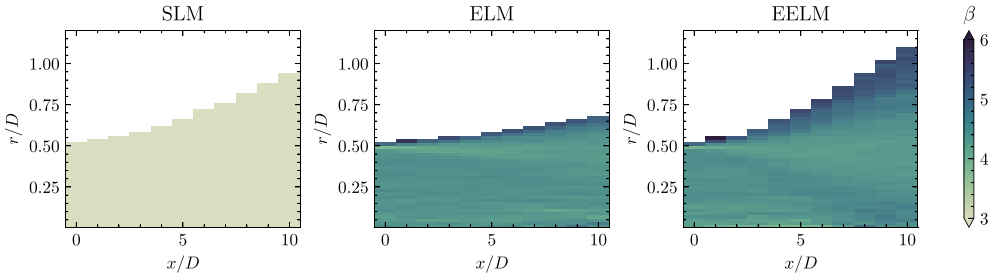

Fig. 9. Radial particle spreading from $x = 0$ to $x = 10\,D$, SLM, ELM and EELM data color-coded by the average aspect ratio β are compared. (For interpretation of the references to color in this figure legend, the reader is referred to the web version of this article.)

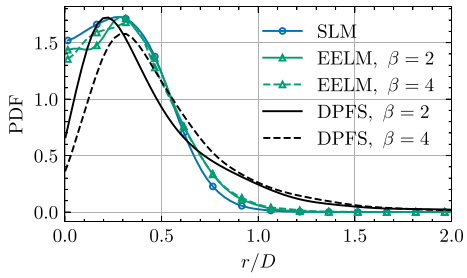

Fig. 10. Probability density function of the radial particle concentration at a location of $x/D = 10$, SLM, EELM, and DPFS data [6] are compared for aspect ratios $\beta = 2$ and $\beta = 4$. The PDF is normalized by the bin area.

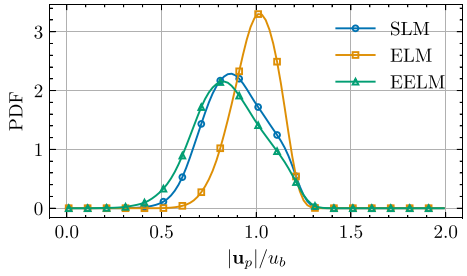

Fig. 11. Probability density function of the particle velocity $|\mathbf{u}_p|/u_b$ at $x/D = 10$, results for different point-particle models are compared.

shows in Fig. 10 a stronger radial spreading than the SLM and EELM and a more pronounced influence of the aspect ratio than the EELM on the radial particle concentration at $x/D = 10$. However, the peak locations agree reasonably well.

5.2.3. Particle dynamics

In the free jet, the PDF of the particle velocity is evaluated at $x/D = 10$. The statistics illustrated in Fig. 11 reveal a comparable reduction in the particle velocity for the SLM and EELM when compared to the pipe flow results and an increasing deviation from the ELM. The velocity predicted by the ELM remains largely unchanged which emphasizes the underprediction of the hydrodynamic force acting on the particles.

For the rotational motion, a larger average particle angular velocity compared to the pipe flow is observed in the near field of the jet. This is attributed to the stronger local velocity gradients and increased turbulent intensity. The relative behavior of the ELM and EELM remains unchanged, as highlighted in Fig. 12 for $x/D = 10$. Note that the values are still one order of magnitude lower than the DPFS data [6].

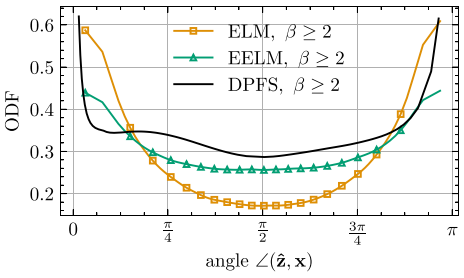

Fig. 13. Orientation distribution function of the particle orientation $\angle(\mathbf{x}, \hat{\mathbf{z}})$ defined by the angle between the streamwise direction $\mathbf{x}$ and the particle's major axis $\hat{\mathbf{z}}$, results for ellipsoidal point-particle models and DPFS [6] for the mean of prolate particles with aspect ratios $\beta \geq 2$ at $x/D = 10$ downstream of the nozzle are compared. The DPFS data have been scaled according to the ODF formulation.

The analysis of the particle orientation in Fig. 13 reveals larger differences between the two ellipsoidal models. The ELM retains a strong preference for an alignment of the major axis with the primary flow direction independent of the streamwise location, whereas a flattening of the distribution is observed for the EELM. Nevertheless, the peaks in the ODF at 0° and 180°, i.e., 0 and π, persist at $x/D = 10$. This behavior is explained by a decrease in the velocity-gradient magnitude, resulting in a stronger contribution of the pitching torque in (23) as well as the transition towards a more uniform flow field further downstream. Despite remaining quantitative differences, the qualitative behavior of the EELM agrees much better with the DPFS results in the jet than in the pipe flow. This highlights the differences between wall-bounded shear flow and the free-shear flow, particularly limitations of the correlations derived for uniform flow past fixed particles and the particle-collision modeling.

In summary, the trends in preferential concentration and translational motion for the free jet are well captured by the EELM when compared with the direct particle-fluid simulations. The overall behavior, i.e., particles with larger aspect ratios move farther in the radial direction, is also reproduced. While differences in the angular velocity persist in the near-field of the jet, the preferential orientation observed in direct particle-fluid simulations is reproduced by the EELM.

Overall, this study highlights the limitations of the investigated point-particle models for non-spherical particles in wall-bounded turbulent flows, since none of the evaluated models provides a satisfactory prediction of the particle motion when compared to DPFS data. This is especially true for the pipe flow. The quality of the PPS models is improved in the free jet although the jet inflow condition is determined by the fully developed pipe flow. It seems that in this non-equilibrium turbulent flow, the history of the inlet distribution fades away faster than in the pipe flow.

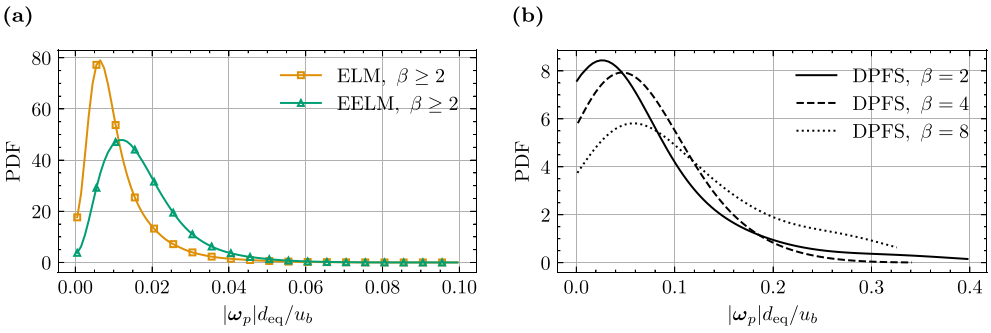

Fig. 12. Probability density function of the particle angular velocity magnitude $|\boldsymbol{\omega}_p| d_{\mathrm{eq}}/u_b$ at $x/D = 10$, (a) results for different point-particle models for the mean of prolate particles with $\beta \geq 2$ and (b) DPFS results [6] for $\beta = 2$, 4, and 8 are compared. Note the different scaling of the x-axes.

6. Conclusion

Coupled Euler-Lagrange simulations are conducted for a particle-laden pipe and free jet flow. Both simulations are performed concurrently. The periodic pipe flow provides the inflow conditions for the jet. This setup ensures consistent inlet conditions for the carrier and dispersed phases. The flow is laden with heavy rigid spherical and ellipsoidal particles with aspect ratios in the range of $1 \leq \beta \leq 8$.

Three point-particle models have been considered to model the dispersed phase: a spherical model, an ellipsoidal model derived under creeping flow conditions, and an ellipsoidal model extended by corrections for finite particle Reynolds numbers through orientation-dependent drag, lift, and torque correlations. The results for the different point-particle models are compared with direct particle-fluid simulation data determined for the same configuration.

The analysis of the pipe flow shows similar predictions for the SLM and EELM, whereas the creeping flow ELM significantly over-predicts the particle velocity. This shows the importance of the finite particle Reynolds corrections. In general, substantial deviations in the preferential particle concentration are observed for all point-particle models when compared with direct particle-fluid simulation (DPFS) data. Discrepancies are also evident in the rotational motion, with up to one order of magnitude lower angular velocities compared to the DPFS data. Although the average orientation angle is approximately 52 °, the ELM and EELM still show, unlike the DPFS solutions, a streamwise preference in the orientation distribution functions. The deviations are caused by the current collision treatment, which is based on a purely reflective model that does not affect the rotational motion. An improved algorithm, taking into account eccentric collisions, should be implemented. Moreover, another reason for the discrepancies is the correlations in the EELM which were derived for uniform flow instead of shear flow.

For the turbulent free jet flow problem, the SLM and EELM show qualitatively good agreement in the translational motion and radial spreading. Both models describe the influence of the particulate phase on the jet development. The EELM also captures tendency for particles with larger aspect ratios to migrate farther in the radial direction, which matches the DPFS results. The rotational dynamics in the near field of the free jet resemble those in the pipe flow. A qualitatively reasonable agreement of the orientation distribution function is observed for the EELM against the DPFS data.

In large-scale simulations of, e.g., combustion chambers, involving particles with sizes on the order of the smallest turbulent scales, where the computational cost of interface-resolved simulations becomes prohibitively high, point-particle simulations that take into account various shapes of the particles remain the method of choice. For the investigated point-particle simulations, the computational cost per time step is predominantly influenced by the flow solver. This remains true for the ellipsoidal point-particle models, despite additional computational costs associated with solving the rotational motion equation and higher memory requirements per particle needed to store the orientation and rotational dynamics. A rough comparison of the computational cost of the point-particle simulations and the direct particle-fluid simulations for the current hardware shows DPFS to be at least a factor of 10 more costly than PPS.

In conclusion, among the investigated point-particle models, the extended ellipsoidal model (EELM) shows a better agreement with the interface-resolved DPFS than the SLM or ELM formulations. It can be anticipated that for particles significantly smaller than the smallest turbulent scales within the flow, the differences between the spherical and ellipsoidal point-particle models become less relevant. The main application for the EELM is to particle-laden flows with particle sizes on the order of the Kolmogorov length scale. However, further improvements of the corrections for the EELM are required. In particular, since the current correlations are derived assuming uniform flow additional corrections for shear flows are to be developed.

CRediT authorship contribution statement

Laurent André: Writing – original draft, Visualization, Validation, Software, Methodology, Investigation, Formal analysis, Conceptualization. **Thede Kiwitt:** Writing – review & editing, Formal analysis, Conceptualization. **Matthias Meinke:** Writing – review & editing, Supervision, Resources, Project administration, Funding acquisition. **Dominik Krug:** Writing – review & editing, Supervision. **Wolfgang Schröder:** Writing – review & editing, Supervision, Resources, Project administration, Funding acquisition.

Declaration of competing interest

The authors declare that they have no known competing financial interests or personal relationships that could have appeared to influence the work reported in this paper.

Acknowledgements

This work has been funded by the German Research Foundation (DFG) within the framework of the SFB/Transregio 129 'Oxyflame' (subproject B2). The support is gratefully acknowledged. Computing resources were provided by the High Performance Computing Center Stuttgart (HLRS) within a Large-Scale Project of the Gauss Centre for Supercomputing (GCS).

Appendix A. Resistance tensors and shape parameters

The linear resistance tensor [10] under Stokes flow conditions for a prolate particle with semi-minor axes $a = b$ and semi-major axis $c = \beta a$ where β is the aspect ratio as well as the resistance tensors for the rotational motion under creeping shear flow according to [11] are given in Table A.2. The corresponding shape parameters following the definition of [44] are summarized in Table A.3.

Table A.2
Resistance tensors for a prolate particle under the assumption of creeping flow.

Tensor	Expression
$\underline{\hat{\mathbf{K}}}$	$16\,\pi\,\beta\,a^3\,\mathrm{diag}\left(\frac{1}{\chi_0+a^2\,\alpha_0}, \frac{1}{\chi_0+a^2\,\alpha_0}, \frac{1}{\chi_0+\beta^2\,a^2\,\gamma_0}\right)$
$\underline{\hat{\mathbf{K}}}_s$	$\frac{16}{3}\,\pi\,\beta\,a^3\,\mathrm{diag}\left(\frac{1-\beta^2}{\alpha_0+\beta^2\,\gamma_0}, \frac{\beta^2-1}{\alpha_0+\beta^2\,\gamma_0}, 0\right)$
$\underline{\hat{\mathbf{K}}}_\zeta$	$\frac{16}{3}\,\pi\,\beta\,a^3\,\mathrm{diag}\left(\frac{1+\beta^2}{\alpha_0+\beta^2\,\gamma_0}, \frac{1+\beta^2}{\alpha_0+\beta^2\,\gamma_0}, \frac{1}{\alpha_0}\right)$

Table A.3
Shape Parameters for prolate particles.

κ	χ_0	α_0	γ_0
$\log\left(\frac{\beta-\sqrt{\beta^2-1}}{\beta+\sqrt{\beta^2-1}}\right)$	$\frac{-a^2\,\beta}{\sqrt{\beta^2-1}}\,\kappa$	$\frac{\beta^2}{\beta^2-1} + \frac{\beta}{2(\beta^2-1)^{3/2}}\,\kappa$	$\frac{-2}{\beta^2-1} - \frac{\beta}{(\beta^2-1)^{3/2}}\,\kappa$

Appendix B. EELM: coefficients and empirical correlation functions

The coefficients and correlation functions for the EELM are derived in [19], and an overview is given below. For Stokes flow, the drag coefficient for the limiting orientations of $\phi = 0°$ and $\phi = 90°$ reads

$$C_{D,\mathrm{Stokes},0}(Re_p, \beta) = \frac{64\,\beta^{2/3}}{Re_p}\,\frac{1}{\chi_0\,/\,a^2 + \beta^2\,\gamma_0}\,, \tag{B.1}$$

$$C_{D,\mathrm{Stokes},90}(Re_p, \beta) = \frac{64\,\beta^{2/3}}{Re_p}\,\frac{1}{\chi_0/a^2 + \alpha_0}\,, \tag{B.2}$$

where the shape parameters χ_0, γ_0, and α_0 are defined in Appendix A. Empirical functions are used to correct these coefficients in (21). The

correction terms read

$$f_{d,0}(Re_p,\beta) = f_{d,SN} + c_{d,1}(\log(\beta))^{c_{d,2}}\, Re_p^{c_{d,3}+c_{d,4}\log(\beta)}\,, \tag{B.3}$$

$$f_{d,90}(Re_p,\beta) = f_{d,SN} + c_{d,5}(\log(\beta))^{c_{d,6}}\, Re_p^{c_{d,7}+c_{d,8}\log(\beta)}\,. \tag{B.4}$$

For the lift coefficient in (22), a coordinate transformation for the inclination angle ϕ is introduced

$$\Psi_\phi(Re_p,\beta) = \frac{\pi}{2}\left(\frac{\phi}{\pi/2}\right)^{f_{l,\mathrm{shift}}(Re_p,\beta)}\,, \tag{B.5}$$

with

$$f_{l,\mathrm{shift}}(Re_p,\beta) = \begin{cases} 1 + c_{l,1}\,\log(\beta)^{c_{l,2}}\,\log(Re_p)^{c_{l,3}} & Re_p > 1\,, \\ 1 & \text{otherwise}\,. \end{cases} \tag{B.6}$$

The maximum lift coefficient corrected for finite Re_p reads

$$C_{L,\max}(Re_p,\beta) = f_{l,\max}(Re_p,\beta)\,\frac{C_{D,\mathrm{Stokes},90} - C_{D,\mathrm{Stokes},0}}{2}\,, \tag{B.7}$$

with

$$f_{l,\max}(Re_p,\beta) = \left(1 + c_{l,4}\, Re_p^{c_{l,5}+c_{l,6}\,\log(\beta)}\right)\,. \tag{B.8}$$

The maximum torque coefficient used in (24) is

$$C_{T,\max}(Re_p,\beta) = \frac{c_{t,1}\log(\beta)^{c_{t,2}}}{Re_p^{c_t,3}} + \frac{c_{t,4}\log(\beta)^{c_{t,5}}}{Re_p^{c_{t,6}+c_{t,7}\,\log(\beta)}}\,. \tag{B.9}$$

The fitted constants for $c_{d,i}$, $c_{l,i}$, and $c_{t,i}$ obtained in [19] are summarized in Table B.4.

Table B.4
Empirical coefficients for the drag, lift, and torque coefficients as derived in [19].

i	1	2	3	4	5	6	7	8
$c_{d,i}$	−0.007	1.0	1.17	−0.07	0.047	1.14	0.7	−0.008
$c_{l,i}$	0.01	0.86	1.77	0.34	0.88	−0.05	–	–
$c_{t,i}$	0.931	0.675	0.162	0.657	2.77	0.178	0.177	–

Data availability

Data will be made available on request.

References

[1] Hamzeh NH, Karami S, Kaskaoutis DG, Tegen I, Moradi M, Opp C. Atmospheric dynamics and numerical simulations of six frontal dust storms in the Middle East region. Atmosphere 2021;12:125. https://doi.org/10.3390/atmos12010125

[2] Shams M, Ahmadi G, Smith DH. Computational modeling of flow and sediment transport and deposition in meandering rivers. Adv Water Resour 2002;25:689–99. https://doi.org/10.1016/S0309-1708(02)00034-9

[3] Steffens P, Berkel L, Gierth S, Debiagi P, Özer B, Maßmeyer A, Nicolai H, Hasse C. LES of a swirl-stabilized 40 kWth biomass flame and comparison to a coal flame. Fuel 2024;372:132098. https://doi.org/10.1016/j.fuel.2024.132098

[4] Intergovernmental Panel On Climate Change (Ipcc), Ed. Climate Change 2022 – Mitigation of Climate Change: Working Group III Contribution to the Sixth Assessment Report of the Intergovernmental Panel on Climate Change. 1st ed. Cambridge University Press; 2023. https://doi.org/10.1017/9781009157926

[5] Guo Q, Chen X, Liu H. Experimental research on shape and size distribution of biomass particle. Fuel 2012;94:551–5. https://doi.org/10.1016/j.fuel.2011.11.041

[6] Kiwitt T, Meinke M, Krug D, Schröder W. Direct particle–fluid simulation of spherical and ellipsoidal particles in turbulent pipe-free-jet flow. Int J Multiph Flow 2026;194:105443. https://doi.org/10.1016/j.ijmultiphaseflow.2025.105443

[7] Lucci F, Ferrante A, Elghobashi S. Modulation of isotropic turbulence by particles of Taylor length-scale size. J Fluid Mech 2010;650:5–55. https://doi.org/10.1017/S0022112009994022

[8] Kuerten JGM. Point-particle DNS and LES of particle-laden turbulent flow – a state-of-the-art review. Flow Turbul Combust 2016;97:689–713. https://doi.org/10.1007/s10494-016-9765-y

[9] Maxey MR, Riley JJ. Equation of motion for a small rigid sphere in a nonuniform flow. Phys. Fluids. 1983;26:883–9. https://doi.org/10.1063/1.864230

[10] Oberbeck A. Ueber stationäre Flüssigkeitsbewegungen mit Berücksichtigung der inneren Reibung. J für reine angew Math (Crelles J) 1876;1876:62–80. https://doi.org/10.1515/crll.1876.81.62

[11] Jeffery GB. The motion of ellipsoidal particles immersed in a viscous fluid. Proc. R. Soc. Lond. A Math. Phys. 1922;102:161–79. https://doi.org/10.1098/rspa.1922.0078

[12] Mortensen PH, Andersson HI, Gillissen JJJ, Boersma BJ. On the orientation of ellipsoidal particles in a turbulent shear flow. Int J Multiph Flow 2008;34:678–83. https://doi.org/10.1016/j.ijmultiphaseflow.2007.12.007

[13] Marchioli C, Soldati A. Rotation statistics of fibers in wall shear turbulence. Acta Mech 2013;224:2311–29. https://doi.org/10.1007/s00707-013-0933-z

[14] Siewert C, Kunnen RPJ, Schröder W. Collision rates of small ellipsoids settling in turbulence. J Fluid Mech 2014;758:686–701. https://doi.org/10.1017/jfm.2014.554

[15] Schneiders L, Meinke M, Schröder W. On the accuracy of Lagrangian point-mass models for heavy non-spherical particles in isotropic turbulence. Fuel 2017;201:2–14. https://doi.org/10.1016/j.fuel.2016.11.096

[16] Zastawny M, Mallouppas G, Zhao F, van Wachem B. Derivation of drag and lift force and torque coefficients for non-spherical particles in flows. Int J Multiph Flow 2012;39:227–39. https://doi.org/10.1016/j.ijmultiphaseflow.2011.09.004

[17] Ouchene R, Khalij M, Arcen B, Tanière A. A new set of correlations of drag, lift and torque coefficients for non-spherical particles and large Reynolds numbers. Powder Technol 2016;303:33–43. https://doi.org/10.1016/j.powtec.2016.07.067

[18] Sanjeevi SKP, Kuipers JAM, Padding JT. Drag, lift and torque correlations for non-spherical particles from Stokes limit to high Reynolds numbers. Int J Multiph Flow 2018;106:325–37. https://doi.org/10.1016/j.ijmultiphaseflow.2018.05.011

[19] Fröhlich K, Meinke M, Schröder W. Correlations for inclined prolates based on highly resolved simulations. J Fluid Mech 2020;901:A5. https://doi.org/10.1017/jfm.2020.482

[20] Van Wachem B, Zastawny M, Zhao F, Mallouppas G. Modelling of gas–solid turbulent channel flow with non-spherical particles with large Stokes numbers. Int J Multiph Flow 2015;68:80–92. https://doi.org/10.1016/j.ijmultiphaseflow.2014.10.006

[21] Fröhlich K, Farmand P, Pitsch H, Meinke M, Schröder W. Particle Reynolds number effects on settling ellipsoids in isotropic turbulence. Int J Multiph Flow 2021;139:103566. https://doi.org/10.1016/j.ijmultiphaseflow.2021.103566

[22] Schneiders L, Günther C, Meinke M, Schröder W. An efficient conservative cut-cell method for rigid bodies interacting with viscous compressible flows. J Comput Phys 2016;311:62–86. https://doi.org/10.1016/j.jcp.2016.01.026

[23] Schneiders L, Meinke M, Schröder W. Direct particle–fluid simulation of Kolmogorov-length-scale size particles in decaying isotropic turbulence. J Fluid Mech 2017;819:188–227. https://doi.org/10.1017/jfm.2017.171

[24] Schneiders L, Fröhlich K, Meinke M, Schröder W. The decay of isotropic turbulence carrying non-spherical finite-size particles. J Fluid Mech 2019;875:520–42. https://doi.org/10.1017/jfm.2019.516

[25] Panahi A, Levendis YA, Vorobiev N, Schiemann M. Direct observations on the combustion characteristics of Miscanthus and Beechwood biomass including fusion and spherodization. Fuel Process Technol 2017;166:41–9. https://doi.org/10.1016/j.fuproc.2017.05.029

[26] Kiwitt TP. Direct particle-fluid simulations of isothermal and non-isothermal turbulent flows. Dissertation, Rheinisch-Westfälische Technische Hochschule Aachen; 2025. https://doi.org/10.18154/RWTH-2025-09382

[27] Siewert C, Kunnen RPJ, Meinke M, Schröder W. Orientation statistics and settling velocity of ellipsoids in decaying turbulence. Atmos Res 2014;142:45–56. https://doi.org/10.1016/j.atmosres.2013.08.011

[28] Institute of Aerodynamics. m-AIA. Zenodo; 2024. https://doi.org/10.5281/zenodo.13350586.

[29] Hartmann D, Meinke M, Schröder W. An adaptive multilevel multigrid formulation for Cartesian hierarchical grid methods. Comput Fluids 2008;37:1103–25. https://doi.org/10.1016/j.compfluid.2007.06.007

[30] Schneiders L, Hartmann D, Meinke M, Schröder W. An accurate moving boundary formulation in cut-cell methods. J Comput Phys 2013;235:786–809. https://doi.org/10.1016/j.jcp.2012.09.038

[31] Niemöller A, Schlottke-Lakemper M, Meinke M, Schröder W. Dynamic load balancing for direct-coupled multiphysics simulations. Comput. Fluids. 2020;199:104437. https://doi.org/10.1016/j.compfluid.2020.104437

[32] Günther C, Meinke M, Schröder W. A flexible level-set approach for tracking multiple interacting interfaces in embedded boundary methods. Comput Fluids 2014;102:182–202. https://doi.org/10.1016/j.compfluid.2014.06.023

[33] Glowinski R, Pan TW, Hesla TI, Joseph DD, Périaux J. A fictitious domain approach to the direct numerical simulation of incompressible viscous flow past moving rigid bodies: application to particulate flow. J Comput Phys 2001;169:363–426. https://doi.org/10.1006/jcph.2000.6542

[34] Wegmann T, Niemöller A, Meinke M, Schröder W. Parallel Eulerian-Lagrangian coupling method on hierarchical meshes. J Comput Phys 2025;521:113509. https://doi.org/10.1016/j.jcp.2024.113509

[35] Maxey MR, Patel BK, Chang EJ, Wang L-P. Simulations of dispersed turbulent multiphase flow. Fluid Dyn Res 1997;20:143–56. https://doi.org/10.1016/S0169-5983(96)00042-1

[36] Fröhlich K, Schneiders L, Meinke M, Schröder W. Validation of Lagrangian two-way coupled point-particle models in large-eddy simulations. Flow Turbul Combust 2018;101:317–41. https://doi.org/10.1007/s10494-018-9933-3

[37] Quintero B, Laín S, Sommerfeld M. Derivation and validation of a hard-body particle-wall collision model for non-spherical particles of arbitrary shape. Powder Technol 2021;380:526–38. https://doi.org/10.1016/j.powtec.2020.11.032
[38] Wedel J, Štrakl M, Hriberšek M, Steinmann P, Ravnik J. A novel particle–particle and particle–wall collision model for superellipsoidal particles. Comp. Part. Mech. 2024;11:211–34. https://doi.org/10.1007/s40571-023-00618-6
[39] Schiller L, Naumann A. Über die grundlegenden Berechnungen bei der Schwerkraftaufbereitung. Z Ver Dtsch Ing 1933;77:318–20.
[40] Sanjeevi SKP, Padding JT. On the orientational dependence of drag experienced by spheroids. J Fluid Mech 2017;820:R1. https://doi.org/10.1017/jfm.2017.239
[41] Nguyen CT, Oberlack M. Comparative study of turbulent round jet flows through direct numerical simulation at medium–high Reynolds numbers. Phys Fluids 2024;36:115145. https://doi.org/10.1063/5.0228993
[42] Chin C, Ooi ASH, Marusic I, Blackburn HM. The influence of pipe length on turbulence statistics computed from direct numerical simulation data. Phys Fluids 2010;22:115107. https://doi.org/10.1063/1.3489528
[43] Michaelides EE, Crowe CT, Schwarzkopf JD, Eds. Multiphase Flow Handbook. 2nd ed. CRC Press; 2016. https://doi.org/10.1201/9781315371924
[44] Brenner H. The Stokes resistance of an arbitrary particle—III. Chem Eng Sci 1964;19:631–51. https://doi.org/10.1016/0009-2509(64)85052-1